



Experimental investigation of the brittle-viscous transition in mafic rocks – Interplay between fracturing, reaction, and viscous deformation

Sina Marti, Holger Stünitz, Renée Heilbronner, Oliver Plumper, Martyn Drury

► To cite this version:

Sina Marti, Holger Stünitz, Renée Heilbronner, Oliver Plumper, Martyn Drury. Experimental investigation of the brittle-viscous transition in mafic rocks – Interplay between fracturing, reaction, and viscous deformation. *Journal of Structural Geology*, 2017, 105, pp.62-79. 10.1016/j.jsg.2017.10.011 . insu-01636815

HAL Id: insu-01636815

<https://insu.hal.science/insu-01636815>

Submitted on 28 Nov 2019

HAL is a multi-disciplinary open access archive for the deposit and dissemination of scientific research documents, whether they are published or not. The documents may come from teaching and research institutions in France or abroad, or from public or private research centers.

L'archive ouverte pluridisciplinaire **HAL**, est destinée au dépôt et à la diffusion de documents scientifiques de niveau recherche, publiés ou non, émanant des établissements d'enseignement et de recherche français ou étrangers, des laboratoires publics ou privés.

**Experimental investigation of the brittle-viscous transition in mafic rocks –
interplay between fracturing, reaction, and viscous deformation**

***Sina Marti**^a, Holger Stünitz^{b,c}, Renée Heilbronner^a, Oliver Plümper^d, Martyn
Drury^d

^a Department of Environmental Sciences, Basel University, Switzerland
(sina.marti@unibas.ch, +41 79 505 81 82, Brombacherstr. 27, 4057 Basel;
renee.heilbronner@unibas.ch)

^b Department of Geosciences, UiT the arctic University of Norway, Norway
(holger.stunitz@uit.no)

^c Institut des Sciences de la Terre d'Orléans (ISTO), Université d'Orléans, France

^d Department of Earth Sciences, Utrecht University, Netherlands (O.Plumper@uu.nl;
M.R.Drury@uu.nl)

Keywords: Rock deformation experiments, Brittle-viscous transition, Dissolution-
precipitation, grain boundary sliding, Polyphase rheology

Abstract

Rock deformation experiments are performed on fault gouge fabricated from
'Maryland Diabase' rock powder to investigate the transition from dominant brittle
to dominant viscous behaviour. At the imposed strain rates of $\dot{\gamma} \sim 3 \cdot 10^{-5} - 3 \cdot 10^{-6} \text{ s}^{-1}$,
the transition is observed in the temperature range of ($600 \text{ }^{\circ}\text{C} < T < 800 \text{ }^{\circ}\text{C}$) at
confining pressures of ($0.5 \text{ GPa} \leq P_c \leq 1.5 \text{ GPa}$). From microstructural observations,
the transition is effected by a switch from brittle fracturing and cataclastic flow, to
viscous dissolution-precipitation creep and grain boundary sliding. Mineral
reactions and resulting grain size refinement by nucleation are observed to be
critical processes for the switch to viscous deformation, i.e., grain size sensitive
creep. In the transitional regime, the mechanical response of the sample is a mixed-
mode between brittle and viscous rheology and microstructures associated with
both brittle and viscous deformation are observed. As grain size reduction by
reaction and nucleation is a time dependent process, the brittle-viscous transition is
not only a function of T but to a large extent also of microstructural evolution.

1. Introduction

Our knowledge about rock strength is largely based on laboratory-derived data. Given the condition that the strength of the lithosphere cannot be greater than that of the constituting rocks and minerals, strength envelopes are constructed, which plot laboratory-derived strength or flow laws for minerals (or rocks) versus depth (as a proxy for pressure and temperature) (e.g. Brace and Kohlstedt, 1980; Kohlstedt et al., 1995; Burov, 2011 and references therein). Following the general consensus that the upper crust deforms dominantly by fracturing and the lower crust and upper mantle by viscous creep, the early strength envelopes were constructed using a constant strain rate, two-mechanism model (e.g., Brace and Kohlstedt, 1980). Frictional rock strength (Byerlee, 1978) is plotted against depth to temperature and pressure conditions, where viscous deformation takes place at lower stresses than frictional sliding. Here, the term 'viscous' refers to temperature and rate sensitive deformation mechanisms such as dislocation and diffusion creep (including pressure solution creep).

Rocks deforming in the brittle field change their mode of deformation from frictional sliding along a discrete plane to distributed cracking at elevated pressures (e.g. Karman, 1911; Kirby and Kronenberg, 1984), because frictional sliding at elevated confining pressures requires higher stresses than those needed to form new cracks. This change from discrete to distributed ('ductile') deformation mode is termed "brittle-ductile transition" (BDT) and is also termed the region of semi-brittle deformation (e.g. Kohlstedt et al., 1995). Towards greater depth, the semi-brittle field is terminated by another transition, which is primarily temperature dependent. This transition is termed the "brittle-plastic transition", where the term 'plastic' denotes a permanent, non-brittle deformation without specifying a particular mechanism (Kohlstedt et al. 1995). The term "plastic" may have different meanings in terms of rheology and deformation processes, so that the for a general temperature- and rate sensitive, pressure-insensitive deformation the more general term 'brittle-viscous' transition (BVT) is preferred and will be used in this text. The introduction of a semi-brittle field to the classical strength envelope predicts a broad transitional field from dominant brittle to dominant viscous deformation.

The onset of viscous deformation (BVT, or, alternatively, an increasing α -factor for the effective pore pressure law at the BDT, according to Hirth and Beeler, 2015) within the Earth's crust is generally associated with the disappearance of earthquake rupture. Where the occurrence of the BVT is considered to be a simple function of pressure and temperature (as proxies for depth), the BVT regime may be considered as the lower depth

limit of the seismogenic zone (e.g. Sibson, 1982, 1984). However, at the BVT several processes are competing: fracturing, frictional sliding, crystal plasticity, and diffusive mass transfer. Given the number of parameters controlling the deformation, the BVT, where both, time-dependent viscous mechanisms and relatively more time-independent brittle and frictional processes significantly contribute to the deformation, is a complex system where temperature, pressure, fluid availability, grain size, strain rate, microstructure, rock composition (i.e. mineral assemblage), and chemical environment control the rheology. As a consequence, it is not surprising that there is a lack of laboratory data characterising the BVT in detail, despite pioneering seminal works by, e.g., Griggs et al. (1960); Heard (1960); Handin (1966); Byerlee (1967, 1968); Tullis and Yund (1977); Brace and Kohlstedt (1980); Carter and Tsenn (1987); and review in Paterson and Wong (2005) and references therein.

In the absence of flow laws for other crustal minerals, the viscous strength of the continental crust was first estimated using a dislocation creep flow law for quartz (Brace and Kohlstedt, 1980). However, large proportions of the lower continental crust, and most of the oceanic crust are of mafic composition and quartz is virtually absent. Strength estimates for these crustal parts could only be assessed since flow law parameters for plagioclase and pyroxene became available (e.g. Mackwell, 1991; Raterron and Jaoul, 1991; Bystricky and Mackwell, 2001; Rybacki and Dresen, 2000; Rybacki et al., 2006; Chen et al., 2006; Dimanov et al., 2003; Dimanov and Dresen, 2005; Dimanov et al., 2007). Most of the data, however, is applicable to high temperature deformation, and experimental studies for mafic rocks at lower temperatures are scarce (e.g. Kronenberg and Shelton, 1980; Shelton et al., 1981; Rutter et al., 1985; Hacker and Christire, 1991; Tullis and Yund, 1987; Getsinger and Hirth, 2014).

One important aspect of the BVT - not represented in the strength envelope plots - is the development of the rheology of sheared rock over time or during a strain history. Fault- and shear zones may show a strain-dependent microstructural evolution, which, in turn, may cause a strain-dependent strength evolution. One of the consequences of such a strain-history-dependent evolution is that fault/shear zones are unlikely to initiate with their final steady state strength. It is frequently seen from natural examples that brittle and viscous deformation can occur

cyclically (e.g. Gratier et al., 2011; Price et al., 2012) or sequentially in time (e.g. Simpson, 1986; Fitz Gerald and Stünitz, 1993; Stünitz and Fitz Gerald, 1993; Trepmann and Stöckert, 2003; Mancktelow and Pennacchioni, 2005; Pennacchioni and Mancktelow, 2007; Füsseis and Handy, 2008; Goncalves et al., 2016; Bukovská et al., 2016).

Relatively little is known about the rheology of fault rocks undergoing the BVT. As fault zones are considered to sustain the highest differential stress values near the BVT, it constitutes a key regime controlling the dynamics of lithospheric fault-zone systems. In this study, we aim to further our understanding of the evolution and the rheology of mafic rocks at conditions where the rocks undergo their BVT. Significant amounts of the global seismic moment occur along faults within the oceanic crust and along subduction zones. A better understanding of the behaviour of mafic rocks at the BVT will potentially aid our understanding of earthquake distribution and seismic hazard in these regions.

Furthermore, in order to address the question of strain dependent rheology, experiments have been performed to various amounts of strain to observe microstructural changes and evolving mechanical properties during fault-/shear-zone formation. One of the aims of this study is to gain insights into the deformation processes active over the BVT in a mafic rock and how initiation and development of fault/shear zones are achieved. Mechanical response is measured and deformation mechanisms are identified in the brittle, the semi-brittle and the viscous field.

2. Methods

2.1 Experimental procedure

2.1.1 Sample material

Experiments were performed on Maryland Diabase (Kronenberg and Shelton, 1980). The Maryland Diabase starting material ([Table 1](#)) has a modal composition (by volume) of ~ Plagioclase (Pl): 57%, Clinopyroxene (Cpx): 32%, Orthopyroxene (Opx): 8%, accessories (Qz, Kfs, Ilm, Mag, Bt, Ap): 3% (mineral abbreviations after Whitney and Evans, 2010). The Pl shows a relatively homogeneous composition of ~ An₆₅₋₇₀ except for a thin rim with a lower Anorthite component of ~ An₅₀₋₅₅. The core to rim area ratio is ~ 83 : 17 (\pm 3). Some of the Cpx grains show a Mg-enriched

core. Pieces of Maryland diabase were crushed with a hand-press and subsequently crushed with an alumina hand-mortar. The resulting powder was dry-sieved to extract the desired grain size fraction $\leq 125 \mu\text{m}$.

2.1.2 Experimental setup and sample assembly

Experiments were performed using two modified Griggs-type deformation apparatus at the University of Tromsø, Norway, at confining pressures (P_c) of ~ 0.5 , 1.0 and 1.5 GPa , at temperatures (T) of 300 , 500 , 600 , 700 and $800 \text{ }^\circ\text{C}$ and with constant displacement rates of $\sim 10^{-8}$ to 10^{-9} m s^{-1} (resulting in strain rates of $\sim 3 \cdot 10^{-5}$ to $3 \cdot 10^{-6} \text{ s}^{-1}$ for homogeneous sample deformation). See [Table 2](#) for a list of experiments and conditions.

The sample assembly is shown in [Figure 1](#). Solid salt is used as confining medium. Inner salt pieces are fabricated from potassium iodide (KI) for experiments at $T \leq 600 \text{ }^\circ\text{C}$ and sodium chlorite (NaCl) for experiments at $T \geq 700 \text{ }^\circ\text{C}$. KI is mechanically weaker than NaCl but shows partial melting at $T > 600 \text{ }^\circ\text{C}$ at the pressures of the experiments, which is to be avoided. Outer salt pieces are always fabricated from NaCl.

The sample consist of a thin layer of crushed rock, produced by placing 0.11 g of MD powder + $0.2 \mu\text{l H}_2\text{O}$ (equals $0.18 \text{ wt.}\%$) between the Al_2O_3 forcing blocks along a 45° pre-cut ([Figure 1](#)). Forcing blocks are cylindrical with a diameter of 6.33 mm . The sample and forcing blocks are placed in a weld-sealed platinum jacket (0.15 mm wall thickness) with a 0.025 mm nickel foil insert. The amount of added water was chosen such that sufficient water is present for solution mass transport processes and mineral reactions, while not inducing mechanical pore pressure effects. No pore pressure effects in the presence of an aqueous fluid were inferred for contents up to $0.5 \text{ wt } \% \text{ H}_2\text{O}$ by Kronenberg and Tullis (1984) and up to $0.3 \text{ wt}\% \text{ H}_2\text{O}$ by Negrini et al. (2013).

During the experiments, approximately 84% of the inelastic axial displacement is accommodated by a shear displacement along the piston-sample interface and approximately 16% by plane strain thinning of the shear zone. The initial shear zone thickness is calculated from the amount of Maryland diabase powder used, the final thickness is measured on thin sections prepared from the samples after the experiment ([Table 2](#)). The shear zone thickness is assumed to decrease linearly

throughout the experiment with increasing piston displacement.

At higher temperatures, the coupling between forcing blocks and rock material in our experiments was found to be poor. Thus, 800 °C experiments were performed using forcing blocks with 6 regularly spaced grooves, ~ 300 µm wide and 150 µm deep, cut into the surface of both, the upper and lower forcing block.

To bring a sample to the desired Pc -T conditions, the σ_1 - and σ_3 -pistons (Figure 1) are advanced in small increments, alternated with increments of heating, Heating is achieved using a graphite resistance furnace and T is measured with a K-type thermocouple positioned adjacent to the centre of the shear zone (Figure 1). When the desired conditions are reached (after 5 to 8 h, duration is longer for higher Pc experiments), shear zone thickness is at ~ 0.83 mm. During the experiment, only the σ_1 -piston is advanced. At the end of the experiment, samples are quenched to 200 °C within 2 minutes while simultaneously retreating the σ_1 -piston to remove the load on the sample. After that, samples are brought back to room conditions by slowly removing the remaining load, temperature and Pc, during ~ 3 h.

2.2 Derivation of stresses and strains

2.2.1 Data recording and processing

During the experiment, the confining pressure, axial load, and displacement are recorded using a digital data-logging system (LabView, 7.1) at a sampling frequency of 1 Hz and temperature is monitored using a proportional integral derivative (PID) controller (Eurotherm) attached to the thermocouple. Temperature is held within ± 1 °C by the controller. There is a vertical T gradient in the sample from the center outwards, ranging from ~ 17 °C/mm at 600 °C (Pec, 2014).

The principal stress σ_3 is considered to be equal to Pc (Eq. 1a), and σ_1 is derived from the measured axial force per sample area.

$$\sigma_3 = Pc \quad (1a)$$

$$\Delta\sigma = \sigma_1 - \sigma_3 \quad (1b)$$

$\Delta\sigma$ is corrected for the decreasing overlap of the forcing blocks (i.e. decreasing

sample area) using a cosine-square approximation to the ACF.

$$ac(i) = \cos^2 (90^\circ \cdot sd(i) / L) \quad (2a)$$

$$\Delta\sigma_{AC} = ac \cdot \Delta\sigma \quad (2b)$$

where $ac(i)$: relative overlap of the forcing blocks; $sd(i)$: shear displacement parallel to the forcing block - sample interface; L : maximum possible shear displacement = diameter of forcing blocks (6.33 mm) / $\cos(45^\circ)$ = 8.95 mm.

The shear and normal stresses, τ and σ_n , supported by the sample inclined at 45° are obtained by Mohr circle construction from $\Delta\sigma_{AC}$. The effective pore fluid pressures in our experiments is assumed to be negligible, i.e. is taken as zero. Axial displacement is corrected for apparatus stiffness. Advancing the σ_1 -piston leads to an increased P_c as a function of the compressibility of the confining medium. The correction is outlined in Richter et al. (2016). Differential stress with the solid salt assemblage in the Griggs rig are usually considered to overestimate rock strength eventually up to 100 MPa (e.g. Green & Borch, 1989).

2.3 Analytical methods

2.3.1 Microscopy

After the experiments, samples are impregnated with epoxy, cut parallel to the shear direction (in some cases also normal to it), and prepared to doubly polished thin sections. Optical light microscope, scanning electron microscope (SEM) and transmission electron microscope (TEM) are used for sample analysis. SEM analyses are performed either with the Zeiss Merlin SEM at Tromsø University, or with a Philips XL30 ESEM at the centre of microscopy (SNI) at Basel University. Chemical analyses are performed using energy dispersive X-ray Spectroscopy (EDS), at 15 kV acceleration voltage and using a ZAF matrix correction.

Transmission electron microscopy (TEM) analyses are carried out at Utrecht University using a FEI Talos 200FX equipped with a high-sensitivity Super-EDX system. TEM images are recorded in bright field (BF), high angular annual dark field (HAADF) and bright field scanning TEM (BF-STEM) modes. BF images are

highly sensitive on crystallographic orientation, whereas contrasts in HAADF images are sensitive to average atomic number (Z-contrast) of the material.

Focussed ion beam (FIB) foils for TEM investigations are prepared in a FEI Helios NanoLab 3G. The FIB foil of the 600 °C experiment is cut perpendicular to both the shear direction and the shear plane. The FIB foils of the 700 and 800 °C experiments are cut parallel to the shear direction and normal to the shear plane.

2.3.2 Image analysis

In this paper, micrographs are always oriented with the shear zone boundaries horizontal and with a dextral sense of shear. The reference coordinate system is shown in [Figure 2](#).

FFT analyses of HR-TEM images: In high-resolution (HR) TEM images where lattice planes of individual crystals are resolved, Fast Fourier Transformations (FFT) can be used to obtain the reciprocal space information akin to a direct diffraction pattern. Lattice fringes are only revealed when the crystal satisfies the diffraction condition. One single HRTEM image of a polycrystalline sample is not likely to reveal lattice fringes in all crystals. Therefore, FFT analysis used to detect diffractions on three HR-TEM images from the same area, with different tilt angles.

EDS profiles: Element concentrations along a line-profile are prepared using the software Fiji (<https://fiji.sc/>). A line-profile of 10 px width is defined, where the value at each point along the profile is an average over these 10 px. In this manner, the noise is reduced. The values are then normalized to the maximum count value (from the whole EDS map) of each element.

Phase Segmentation: Mineral phase segmentations are performed on BSE contrast SEM images. Phases are differentiated by their different Z-contrast using grey-level slicing. As Pyroxene (Px), Amphibole (Amph) and Zoisite (Zo) have similar Z-contrasts, manual post-processing is necessary to properly segment these phases.

Shape and orientation of shear bands: Shear bands and larger shear fractures are digitized manually on BSE contrast SEM images. The x-y coordinates of the outlines

are measured, smoothed (to remove digitizing artefacts) and exported using the program Fiji and analysed with the SURFOR program (Panozzo Heilbronner, 1984; Heilbronner and Barrett, 2014). The SURFOR results yield an orientation distribution function (ODF) of boundary segments of the analysed structures and is presented as a rose diagram. Shear band thicknesses were determined by dividing the digitized shear bands into approximately straight segments, using Fiji to extract the best fit ellipse of each segment and using the short axis of the ellipses as proxy for the shear band thickness.

Grain size and shape: Grain boundaries are traced manually on SE- and BSE- SEM images or on BF TEM images. The resulting grain maps are analysed with Fiji to derive the grain areas and the x-y coordinates of grain boundaries. The area equivalent diameters are calculated and grain size distributions are presented as histograms of equivalent diameters (d_{equ}). Using a kernel density estimate (MATLAB function 'ksdensity'), the mode of the distribution is determined. Grain shape analyses are performed using the SURFOR program.

3. Results

Samples at $T \leq 600$ °C develop similar microstructures and we therefore focus in this paper on the evolution from 600 – 800 °C. Reference frames of image orientation and angles are explained in Figure 2a, b; terminology used when describing stress-strain curves is shown in Figure 2c. Shear strain is always given as apparent shear strain γ_a (for calculation, see Appendix).

3.1 Mechanical data

3.1.1 Stress-strain curves

Shear stress vs. apparent shear strain curves are shown for T of 600 °C, 700 °C and 800 °C and P_c of 0.5, 1.0 and 1.5 GPa (Figure 3a). Samples at 600 and 700 °C show a positive dependence of τ on P_c between 0.5 and 1.0 GPa.

The comparison of the stress-strain data for 700 °C experiments between 1.0 and 1.5 GPa P_c shows that the yield point occurs at relatively similar values. The 1.5 GPa P_c experiments however, unlike all other experiments, show hardening at 700 °C until $\gamma_a \sim 2.3$ where stresses stay at approximately constant levels thereafter.

At 800 °C, sample strength is significantly lower than in lower T experiments and within the variability between individual runs, no strength dependence on P_c is detected. 800 °C experiments show a gradual weakening after peak stress and reach a quasi-steady state at a $\dot{\gamma}_a \sim 4$ onwards (Figure 3a). Note also the lower slope of the initial loading part of the stress-strain curve at 800 °C compared to lower T experiments. Samples at 800 °C deform at stresses below the Goetze criterion (the condition of $\Delta \sigma = P_c$, which is taken as the upper $\Delta \sigma$ -limit of plastic or viscous deformation; Kohlstedt, 1995. In our samples, which are oriented at 45° to σ_1 , $\Delta \sigma = 2 \cdot \tau$). At lower temperatures, all sample deform at $\Delta \sigma$ clearly above the Goetze criterion.

3.1.2 Mohr Circle construction

From Mohr circle constructions (Figure 3b), the positive pressure dependence of strength at 600 °C is clearly visible. Apparent friction coefficients (μ') derived from the Mohr circles yield a value of $\mu' = 0.44$. Experiments at 600 °C and 700 °C, 0.5 GPa P_c reach Byerlee's relationship (Byerlee, 1978) at 'yield', whereas at 1.0 GPa, the stresses at both 'yield' and flow stay below it. At $P_c \geq 1.0$ GPa, and $T \geq 700$ °C, shear stresses are pressure insensitive with an apparent friction coefficient of $\mu' = 0.05$ at 700 °C. No " μ " was determined for 800 °C experiments, due to the variability in the stress values and the sensitivity of the fitted " μ " to low slopes. However, whereas 'yield' stresses do not show any significant pressure dependence, quasi-steady state values reach lower values in the lower P_c experiments at 800 °C.

3.1.3 Stress exponents

Combining constant displacement rate and displacement rate stepping tests, a stress exponent n is determined as

$$\tau \propto \dot{\gamma}^{1/n} \quad (3)$$

where τ : shear stress and $\dot{\gamma}$: shear strain rate. To assess the influence of different data correction routines on calculated stress exponents n , some of our data is

calculated with different published correction routines, to show their influence on the determined stress exponents. The corrections compared are:

1) 'R16': Data correction described in Richter et al. (2016). The same procedure for stress calculations is followed in this paper .

2) 'R16 + H&K10': Data correction after Richter et al. (2016) with the stress correction for the solid-salt assembly after Holyoke III and Kronenberg (2010).

3) 'P12': Data correction described in Pec et al. (2012).

4) 'P12 + H&K10': Data correction after (Pec et al., 2012) with the stress correction for the solid-salt assembly after (Holyoke III and Kronenberg, 2010).

n values are determined for experiments performed at $T = 300\text{ °C}$, $P_c = 0.5\text{ GPa}$; $T = 500\text{ °C}$, $P_c = 1.0\text{ GPa}$; $T = 700\text{ °C}$, $P_c = 1.0\text{ GPa}$ and $T = 800\text{ °C}$, $P_c = 1.0\text{ GPa}$ (Figure 4). For $T \leq 500\text{ °C}$ n is large with values > 19 , n for 700 °C experiments is significantly lower with a value of 5.6 and n at 800 °C is as low as 1.9. The n values determined from different data correction conventions from the literature vary by 16 – 27% (Figure 4b). For example for the $T = 800\text{ °C}$, $P_c = 1.0\text{ GPa}$ experiments, a range of n values from 1.6 – 1.9 arises from different data treatment routines.

3.2 Microstructures

3.2.1 Overview

Strain in experiments at all P_c - T conditions localizes into a network of shear fractures and/or shear bands. The term 'shear band' is used to refer to a zone (with a certain thickness) of high strain accumulation, without any implication of a specific deformation mechanism. As opposite to a 'shear fracture', which is accommodating displacement along a plane without any obvious distribution of strain within a volume (at SEM resolution).

The microstructures developed at different temperatures are systematically different (Figure 5). At 600 °C , the microstructure is dominated by brittle deformation. Fracturing is extensive and a foliation (S), defined by elongated aggregate shapes, develops due to cataclastic flow (Figure 5a, b). Larger shear displacements are accommodated along shear fractures and shear bands, usually in Riedel shear (R_1) orientation. Grain size reduction occurs via pervasive micro-fracturing (Figure 5b). No obvious strength difference between Pl and Px is

observed, as interpreted from the similar degree of fracturing and aggregate elongation of the two phases. In rare occasions, delicate pore trails are seen where fractures are partially healed, potentially indicating limited solution mass transfer (Figure 5c).

The microstructures in 700 °C experiments are discussed for the case of $P_c = 1.0$ and 1.5 GPa. At 700 °C, fracturing of (especially Px-) porphyroclasts is still observed and a weak foliation (defined by elongated aggregate shapes) forms partly by cataclastic flow (Figure 5d). Strain is localized in a network of thin (~ 5 – 15 µm wide) shear bands in C' orientations, cross-cutting the foliation (Figure 5d, e). These shear bands consist of small ($\ll 1$ µm) grains of mainly Pl, Amph and Zo (Figure 5e). Amph and Zo are not part of the starting material and represent syn-kinematic reaction products. The reaction to Amph occurs preferentially along zones of localized deformation such as fractures within Px clasts and along shear bands (Figure 6). The reaction to Zo and more albitic Pl occurs throughout the samples, but small Zo needles predominantly occur in shear bands. Both, the Amph and Zo forming reactions are observed at $P_c = 1.0$ and 1.5 GPa, but occur more extensively at 1.5 GPa.

At 800 °C broad shear bands form, separating low strain lenses between them (Figure 5f). Shear bands are recognized by small grain sizes and a fine-scale compositional layering defining a foliation (Figure 5g). Fracturing is only minor represented in the microstructure but can still be observed. Mineral reactions occur pervasively throughout the sample (i.e. are not restricted to high strain zones) but are more abundant in shear bands compared to low strain lenses. Amph either grows as coronas around Px grains or as aggregates within shear bands (Figure 5g) and has a composition between Mg-Hornblende to Tschermakite (Amph classification after Hawthorne et al., 2012). Zo grains occur as small needles within Pl clasts or within shear bands. Grain sizes in shear bands are usually < 1 µm. Experiments at 800 °C and 1.5 GPa P_c show very similar microstructures but the Amph and especially Zo reaction are more abundant at the higher P_c conditions.

Some melting is observed at 800 °C (melt vol.-% of total sample vol. ≤ 2), where the melt is mainly seen to form small pockets situated in extensional sites between larger porphyroclasts. No melt bands or shear-parallel melt layers are observed.

The geometry of strain localization changes over the temperature range from 600 – 800 °C (Figure 7). Shear bands and shear fractures at 600 °C tend to be few, with large displacements. At 700 °C, shear bands are more abundant, shorter and more anastomosing compared to the lower T experiments. Fractures with larger displacements are less abundant but still observed. At 800 °C, shear bands are broad and form an anastomosing network. Generally no shear fractures with any significant amount of displacement are observed at 800 °C. The preferred orientations of shear bands and shear fractures with respect to the load axis increases from 30° at 600 °C (or 15° towards the shear zone boundaries) to 42° at 800 °C (or 3° towards the shear zone boundaries; Figure 7).

3.2.2 Shear bands formed in low T experiments

Shear bands at 600 °C usually have a thickness of ~2 to 10 µm (Figure 7b) and occur both, along parts of the sample-forcing block interface and traversing the sample. The shear bands are either formed by ultra-cataclasites (type-I shear bands) or by a material that shows flow structures, seen by perturbation of a micron- to sub-micron scale compositional layering (type II shear bands) (Figure 8a). There is a clear and relatively abrupt grain size gradient over a few microns from the lower strain areas into the type-II shear bands. Whereas the material in the low strain domains is usually pervasively fractured, no fractures or grain fragments are resolved within shear bands (at SEM resolution). A type II shear band as shown in Figure 8a has been studied in more detail by TEM. The material in the lower strain domains that border the shear bands consists of larger (>100 nm) angular Pl fragments and the boundary to the shear band material is sharp (Figure 8b). The shear band itself is composed of nano-crystalline and amorphous material in lenticular aggregates and layers, both with fairly sharp boundaries. Some crystals, identifiable by their darker appearance due to diffraction, are observed within the amorphous layers (Figure 8b - d). Lattice planes, seen in high-resolution BF HRTEM images and detected in FFT images show that the amorphously appearing layers still contain nano-crystals (Figure 8d).

3.2.3 Shear bands formed in intermediate T experiments

Figure 9 presents microstructures from shear bands developed at 700°C, 1.0 GPa. At these 700 °C and P_c of 1.0 and 1.5 GPa conditions, shear bands are fully crystalline and mainly composed of fine-grained Pl and Amph (Figure 9c). Pl grain sizes are on the order of ~100 – 200 nm (Figure 9b; 12). Figure 9e shows the result of TEM EDS analysis over an area containing a small Pl porphyroclast surrounded by fine-grained Pl in the shear band. Plotting the relative amounts of the elements Si, Ca and Al along a profile from the porphyroclast into the fine-grained matrix shows slightly higher Al and Ca contents and lower Si content in the porphyroclast compared to the Pl within the shear band.

3.2.4 Shear bands formed in high T experiments

Shear bands formed at 800 °C (P_c = 1.0 and 1.5 GPa) are fully crystalline. The typical microstructure shows fine-grained Pl interlayered with Amph (+Qz) (Figure 10a, c) and a close-up on the Pl grains shows ‘diamond shaped’, largely defect-free grains with a weak shape preferred orientation (Figure 10b; 11). The mean axial ratio of grains is $b/a = 0.64$ and grain sizes are on the order of ~ 0.15 – 0.50 μm (Figure 12). Pore space along grain boundaries is almost absent and grain boundaries are tight (Figure 10b; 11a). Pl grain boundaries show a strong preferred orientation in two maxima ~ 10 – 30° away from the shear plane in both directions (Figure 11). Aligned grain boundaries are frequently observed, where relatively straight grain boundaries can be traced continuous over several neighbouring grains (Figure 11c). The ODF of grain boundary segments is weakly anisotropic with a monoclinic shape, consistent with the global dextral sense of shear.

3.2.5 Grain size distribution of plagioclase in shear bands formed in 700 – 800 °C experiments

Figure 12 presents grain size distributions (GSD) measured from Pl grains within shear bands formed at 700 and 800 °C. Due to the small grain sizes in shear bands at 700 °C, it is difficult to distinguish individual grains. The best results were obtained from SE SEM images of broken surface as shown in Figure 9b. For the 800 °C experiments, grain maps were produced from both TEM and SEM images. Size distributions obtained from TEM and SEM images are similar and the GSD

presented in Figure 12b is measured on Pl grains from TEM images (similar to those shown in Figure 10). The GSD in Figure 12a is measured from grains segmented on SEM images of broken surfaces of a shear band top-view (Figure 9b), thus from a quasi-3D view, whereas the GSD in Figure 12b is from the 2D section of grains measured from a FIB foil in the TEM. Consequently, the two GSD are not fully comparable but yield a semi-quantitative measure of the grain size differences in shear bands between 700 and 800 °C experiments. The size distribution developed at 700 °C is narrow and > 80% of all grains are within 0.11 – 0.25 µm. The mode of the calculated kernel density estimate fit lies at 0.17 µm. The GSD at 800 °C is somewhat broader and > 80% of all grains are within 0.15 – 0.50 µm with a mode of the kernel density estimate calculated fit at 0.30 µm.

3.2.6 Shear band evolution with strain in 800 °C experiments

Figure 13 presents the evolution of shear bands at 800°C, as observed from experiments performed to different amounts of bulk strain, from peak stress ($\gamma_a \sim 0.7$) to a max of $\gamma_a \sim 6.8$. At peak stress, initial shear localization occurs mainly along favourably oriented grain- and phase boundaries. These initial zones are short ($\sim 100 - 200 \mu\text{m}$), distributed (not interconnected) and make an angle of $\sim 27^\circ$ with the load axis. From the microstructure it is apparent that these structures are often dilatant: minor melt segregations, microfracturing and nucleation of new grains/phases such as Amph and Pl are observed (Figure 14). With increasing strain, the initial shear bands start to connect by the formation of interconnected zones of fine-grained material. These zones make a smaller angle to the shear zone boundaries (or $\sim 39^\circ$ with respect to the load axis) and have a width of $\sim 10 - 20 \mu\text{m}$. At a shear strain of $\gamma_a \sim 4$, a network of anastomosing shear bands has formed, with $\sim 3^\circ$ with respect to the shear zone boundaries (i.e. 42° to the load axis). The main shear band strand has a thickness of 50 – 150 µm. This microstructure coincides with the attainment of a quasi-steady state in the mechanical data (Figure 13a, b). With increasing strain, the vol.-% of shear bands increases. Irrespective, sample strength varies only slightly between $\gamma_a \sim 4$ to 6.8 despite the significant increase in vol.-% of shear bands (Figure 13b, c).

3.2.7 Shear band orientation from peak stress to higher strains

Figure 15 shows the difference of shear band orientation at peak stress (~ coinciding with initiation of localization) and at higher strains (at quasi-steady state), as a function of temperature. Initial shear bands at all temperatures show the same preferred orientation, with 27° towards the load axis. This orientation stays relatively constant at ~ 30° in 600 °C experiment, but angles increase to 33° at 700 °C and 42° at 800 °C.

4. Discussion

The strains attained in our experiments are insufficient to attain full microstructural steady state. However, it is expected that the mechanical data reaches quasi-steady state values. The inferred rheology of the samples (e.g. as approximated by the determined stress exponents) always represents a bulk sample rheology, caused by combined mechanisms of deformation and their different rates in low strain domains and shear bands.

4.1 Deformation mechanisms

4.1.1 low *T* experiments

At 600 °C, displacement is mainly accommodated by cataclastic flow. The mechanical data shows a clear positive dependence of sample strength on P_c (Figure 3a, b). High n values of ~20 (Figure 4) are in accordance with dominant brittle deformation and frictional sliding, as it is observed from the microstructure (Figure 5b). Some viscous component of deformation may be indicated by the fact that the n values are not as high as could be expected for purely frictional behaviour.

Displacement in 600 °C experiments is localized in a network of shear fractures and fine-grained shear bands (Figure 5a, b; 7), some of which contain amorphous material (Figure 8). The angles of shear bands and shear fractures to the load axis (~27° - 30°, Figure 15) are in accordance with brittle Riedel (R_1) structures.

The area-% of shear bands in the thin section is about 1 – 2%. As an upper-bound estimate, if all displacement were to be accommodated by the shear bands, the strain rate $\dot{\gamma}$ within them would be on the order of

$$\dot{\gamma} = 10^{-5} \text{ mm s}^{-1} / (0.64 \text{ mm} \cdot 0.02) \approx 8 \cdot 10^{-4} \text{ s}^{-1} \quad (3)$$

which is the applied displacement rate divided by 2% of the approximate shear zone thickness. Although the strain rate within the shear bands is likely to be high, it stays well below seismic rates.

Partly amorphous shear bands as we observe them during aseismic brittle faulting have previously been described (e.g. Yund et al., 1990; Goldsby and Tullis, 2002; Janssen et al., 2010; Pec et al., 2012, 2016). Our TEM analyses show that the shear bands consist of amorphous material, with layers and lenses of nano-crystalline material (Figure 8). A clear material difference is seen between Pl and Px, where Pl preferentially becomes amorphous and Px remains largely crystalline, with very small sizes (< 50 nm, Figure 8c). This is similar to the results of Pec et al. (2012, 2016) or Yund et al. (1990): In their granitoid sample material amorphous shear bands form extensively within the feldspatic material.

The boundaries between shear bands and host rock in our samples are sharp, even on the nano-scale (Figure 8b). It appears from the microstructure that crystalline material is comminuted to a certain grain size (< 50 nm) and below that, amorphization (mainly of the Pl) is effective. (Pec et al., 2012, 2016) discuss different possible formation mechanism for their amorphous material and conclude that the most likely mechanism is a type of mechanical amorphization, i.e. high defect densities until crystallinity is lost. Feldspars appear to be particularly susceptible to this process, as also supported by this study. The rheology of these (partly-)amorphous shear bands, however remains yet unclear.

4.1.2 High *T* experiments

At 800 °C, there is a significant difference in rheology compared to lower *T* experiments: differential stresses at 800 °C are half as high as at 700 °C and stay always below the Goetze criterion (Table 2; Figure 3a). Initial stress increase during sample loading (before peak stress) shows lower slopes at 800 °C (Figure 3a), indicating a larger component of viscous deformation early in the experiment. The microstructure at 800 °C is dominated by mineral reactions and strong grain size refinement (Figure 5f, g; 10). The grain size within shear bands ranges mainly between 0.15 – 0.50 µm for Pl (Figure 12b), with similar sizes for Amph and Zo.

Grain size reduction takes place mainly by nucleation of new grains in conjunction with mineral reactions and potentially aided by strain energy reduction by replacing old, defect-rich porphyroclasts by new defect-free grains. The small grain sizes facilitate a grain size sensitive creep mechanism, where the strain rate is proportional to d^{-m} (e.g. Ashby and Verrall, 1973; Coble, 1963; Rutter, 1976), where d is the grain size and m the grain size exponent. Diffusion creep and grain boundary sliding (GBS) are known to only leave few microstructural traces of their activity. However, aligned grain boundaries, equant to weakly anisotropic grain shapes, and low internal defect densities of grains are microstructures characteristic for GBS and diffusion creep (e.g. Elliott, 1973; Boullier and Gueguen, 1975; Gifkins, 1976; Drury and Humphreys, 1988; Kilian et al., 2011; Drury et al., 2011). The shear bands consist of small, elongated hexagonal grains, whose grain boundaries can be contiguous over several grain diameters (Figure 11). The contiguous grain boundaries are well orientated for sliding in all orientations. As the experiments are performed with H₂O present, dissolution-precipitation creep (DPC) is interpreted to be the dominant form of diffusion creep. DPC needs to be accommodated by some GBS (Lifshitz sliding of Langdon 2006), but the main strain contribution in very small sized aggregates may take place by GBS, where diffusive mass transport accommodates shape changes (Rachinger sliding of Langdon 2006). As both processes are closely linked and interconnected, the term DPC includes both, diffusion creep and GBS. DPC as a dominant deformation mechanism is in accordance with the low observed stress exponents of $n \sim 1.9$. Usually, stress exponents for diffusion creep are expected to be close or equal to 1 (e.g. Ashby and Verrall, 1973; Coble, 1963; Karato, 2008, Kohlstedt and Hansen, 2015; Paterson, 2013), but higher n values have been suggested for DPC, depending on the driving potentials or chemical potential gradients along the grain contact area (e.g., Gratier et al. 2009, 2013). In low strain domains grain sizes are large and DPC will not be an efficient deformation mechanism in these. Frictional sliding may be active in the low strain domains (but not dominant), increasing the stress exponent of the bulk sample to $n = 1.9$. Diffusion creep as viscous deformation mechanism has previously been suggested for experimentally deformed basaltic material (under water added conditions) by e.g. Rutter et al. (1985); Getsinger and Hirth (2014), whereas Rutter

et al. (1985) state more in detail, that they interpret DPC together with GBS to be the dominant deformation mechanism.

4.1.3 Intermediate temperature experiments

The microstructure at 700 °C shows characteristics of both DPC (including GBS) and cataclastic flow. Cataclastic flow thereby is mainly observed to contribute to deformation in low strain lenses (Figure 5d; 6). In shear bands, the similar microstructures as in shear bands at 800 °C suggest that DPC is the dominant deformation mechanisms in shear bands at 700 °C too. The main difference between 800 and 700 °C is the somewhat smaller grain sizes in shear bands at 700 °C (Figure 12).

Fracturing at 700 °C is subordinate within shear bands. Fracturing and cataclasis are expected to produce a wide range of grain sizes with angular grain shapes (e.g. Stel, 1981; Storti et al., 2003; Keulen et al., 2007), unlike the observed microstructure. TEM-EDS mapping also reveals a compositional difference between Pl porphyroclast and fine-grained shear band Pl (Figure 9), which is further evidence that the plagioclase grains within the shear bands are not a result of fracturing but rather result from neocrystallization. The chemical differences are small but the coupled Al+Ca decrease with a Si increase from the clast to the shear band is consistent with a change towards lower anorthite content in the matrix Pl of the shear band. The measured change in Pl chemistry between porphyroclasts and fine-grained shear band Pl also excludes subgrain rotation recrystallization and instead points to nucleation as means of grain size reduction.

However, a brittle precursor to the shear bands at 700°C is possible, interpreted from the initiation of shear bands with the same low angle towards the load axis as in the brittle dominated 600°C experiments (Figure 15), as well as by the similar sample strengths for 600 and 700°C experiments. Due to the low strains at shear band initiation (~ at peak stress) it is, however, difficult to identify from the microstructure if and in which proportions viscous or brittle processes contribute at the point of initiating strain localization.

At 700 °C, sample strength as seen from the stress-strain curves is comparable to the 600 °C experiments (Figure 3a) with a significantly lower stress sensitivity on strain rate ($1/n$) ($n = 5.6$ at 700 °C, $n > 19$ at $T < 600$ °C; Figure 4a). The stress

exponent of 5.6 is just slightly higher than what would be typical for dislocation creep ($n = 3$ to 5; Karato, 2008; Paterson, 2013; Kohlstedt and Hansen, 2015), but none of the microstructures indicate evidence for crystal plasticity. Rather, the intermediate n -value is interpreted to result from a combination of predominantly brittle (n -values of 19.5 and higher) and viscous processes ($n \sim 1.9$), as it is observed in the microstructure.

4.1.4 Summary of deformation mechanisms

The dominance of viscous deformation at 800 °C, and of brittle deformation at 600 °C is evident, both from the mechanical data and the microstructure. Samples deformed at 700 °C are an intermediate case, where strain is localized into shear bands which are interpreted to deform with a viscous deformation mechanism but with stress-strain curves and strengths more like the brittle-dominated 600 °C samples (Figure 3a).

Shear bands formed in 700 °C experiments, like the shear bands at 800 °C, are interpreted to accommodate strain mainly by DPC and GBS. However, low strain lenses at 700 °C show abundant microfracturing and a contribution of cataclastic flow to deformation. The stress exponent is considerably lower at 700 °C than for lower T experiments (Figure 4a), indicating an increased viscous component to the rheology at 700 °C. The stress exponent of $n = 5.6$ for 700 °C experiments is interpreted as a mixed mechanical response determined by the rheology of viscously deforming shear bands and partly frictional/cataclastic low strain lenses. The transition from dominantly brittle deformation to dominantly viscous flow in our experiments is seen to initiate with the dominance of solution-mass transport. Mineral reactions and nucleation lead to grain size reduction and thus strongly enhance the strain rate of grain size sensitive creep mechanisms. For our imposed experimental displacement rates, the transition occurs around 700 °C (although not fully P_c insensitive). In deformation experiments on whole-rock cores of Maryland Diabase at conditions similar to ours, Kronenberg and Shelton (1980) observed a brittle-viscous transition in their samples around 700 °C for a $P_c = 1.0$ GPa, comparable to our observations. However their strain rate was approximately one order of magnitude lower.

In our experiments, the influence of P_c is less pronounced compared to that of the temperature. Increasing the P_c at, e.g., 600 °C does not lead to a transition to more viscous behaviour. At 700 and 800 °C, the main effect of increasing the P_c is the formation of a higher abundance of reaction products. This indicates a rate-enhancing effect of increasing P_c on solution-mass transport processes and/or reaction kinetics, e.g., by a greater overstepping of reaction boundaries for pressure sensitive reactions.

4.2 Microstructural evolution and its influence on bulk rheology

4.2.1 Shear band evolution

As seen from 800 °C experiments, shear bands are widening and increase in vol.-% with increasing strain (Figure 13), caused by the on-going process of mineral reactions and nucleation, leading to the replacement of old, coarser-grained porphyroclasts by new, sub-micron sized grains. Shear band vol.-% stays relatively low in 700 °C experiments for the strains achieved, and interconnectivity is much lower than at 800°C (e.g. Figure 7). From the mechanical data it is seen that 700 °C experiments still show a large influence of brittle deformation, which is attributed to the low volume percentage, unfavourable orientation (not parallel to shear zone boundary but inclined against it with $\sim 7^\circ$), and poor interconnectivity of shear bands. With increasing shear band widening, the viscous rheology of the shear bands at 700 °C is expected to eventually become more dominant.

As reaction and diffusion rates are lower at lower T , more time (or equivalently strain) is needed in the case of the 700 °C experiment to attain a connected network of shear bands as it is observed at 800 °C. However, the positive feedback between fracturing and reaction kinetics (as seen from extensive mineral reactions along microfractures in 700 °C experiments, Figure 6) aids the microstructural change, i.e. grain size reduction by reaction and nucleation, and appears to be an important mechanism in switching from dominant brittle to more viscous rheology.

Comparing the orientations of shear bands formed at different T (Figure 7) it is apparent that the orientations are less favourable for bulk shear displacement in 600 and 700 °C compared to 800 °C experiments, due to the higher inclination of shear bands to the shear zone boundaries. Thus, shear band orientation is an

additional factor determining how the weak phase controls the rheology (cf. Gerbi et al., 2016).

4.2.2. Shear band influence on bulk rheology in high- T experiments – estimating flow stresses in shear bands from plagioclase diffusion creep flow law

The shear band evolution in 800 °C experiments shows an increasing dominance in shear band orientations (sub-)parallel to the shear zone boundaries (Figure 13) with increasing shear band widening and interconnection. That is, the shear band network evolves into geometrically more favourable orientations. Sample strengths, however, remain relatively high, with shear stress values of $\tau > 190\text{MPa}$ (Table 2; Figure 3a). Additionally, a quasi-steady state in the stress-strain curves at $\gamma_a \gtrsim 4$ is reached, disregarding a still increasing shear band vol.-%. These observations again suggest that the bulk sample rheology is not simply determined by the rheology of the shear bands.

For our experimental samples, the imposed displacement rate, temperature and the grain size within shear bands are known. At 800°C, where dissolution precipitation creep is interpreted to dominate the deformation, we can attempt to calculate expected stresses within shear bands for the given conditions. At present, however, the lack of, e.g., mineral solubility data and properties of grain boundary fluid films does not allow to calculate strain rates from common dissolution precipitation creep flow laws at the elevated P_c/T conditions of our experiments. We use a simplified approach to estimate the shear band rheology by applying the flow law of Rybacki and Dresen (2000) (shortened as ‘RD00’) for diffusion creep in feldspars, as has been done previously by e.g. Getsinger and Hirth (2014). The flow law of RD00 has the form:

$$\dot{\varepsilon} = A \cdot \Delta\sigma^n \cdot d^{-m} \cdot \exp\left(-\frac{Q}{RT}\right) \quad (5)$$

where A : constant, $\Delta\sigma$: differential stress, n : stress exponent (usually ~ 1), d : grain size, m : grain size exponent, Q : activation energy, R : universal gas constant, T : temperature.

Under the assumption that the shear bands accommodate the majority of the deformation, a shear strain rate of $\sim 1 \times 10^{-4} \text{ s}^{-1}$ is assumed for them. This is derived from the imposed displacement rate, $\sim 1 \times 10^{-5} \text{ mm s}^{-1}$ divided by the cumulative shear band thickness, $\sim 8 \times 10^{-2} \text{ mm}$ (which is 10 – 20% of the total sample thickness at quasi-steady state in the mechanical data, e.g. [Figure 13](#)). Using the RD00 flow law for diffusion creep in a wet plagioclase aggregate, we use a strain rate of $1 \times 10^{-4} \text{ s}^{-1}$, a grain size range of $0.15 - 0.50 \text{ }\mu\text{m}$ and $T = 800 \text{ }^{\circ}\text{C}$. To compare our shear strain rates to the axial shortening strain rates of the flow law, the conversion from axial shortening to simple shear strain rates after Schmid et al. (1987) is used, reformulating Eq. (5) to :

$$\dot{\gamma} = A \cdot \sqrt{3}^{(n+1)} \cdot \tau^n \cdot d^{-m} \cdot \exp\left(-\frac{Q}{RT}\right) \quad (6)$$

$\dot{\gamma}$: shear strain rate, A : constant, n : stress exponent = 1, τ : shear stress, d : grain size, m : grain size exponent = 3, Q : activation energy, R : universal gas constant, T : temperature.

Solving Eq. (6) for shear stresses, they are calculated as:

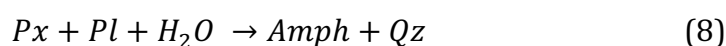
$$\tau = \exp\left(\log\left(\frac{\dot{\gamma}}{A \cdot \sqrt{3}^{(n+1)} \cdot d^{-m}}\right) - \left(\frac{-Q}{R \cdot T}\right)\right) \quad (7)$$

Resulting shear stresses are between $0.4 - 16 \text{ MPa}$. That is one to almost three orders of magnitude lower than measured in the mechanical data. Conversely, if Eq. (6) were used to calculate the strain rate for the given T and d , with the measured $\tau = 200 \text{ MPa}$, strain rates of 1×10^{-3} to $5 \times 10^{-2} \text{ s}^{-1}$ would result. Our experimental samples contain higher wt.-% H_2O compared to the samples of Rybacki and Dresen (2000), which is likely to have a marked effect on the rate of DPC. Nonetheless, despite some uncertainties in the application of the RD00 flow law, the results are expected to yield values within the expected order of magnitude for DPC. The calculated stresses for the shear bands thus suggest that the elevated bulk sample strengths of $\tau \approx 200 \text{ MPa}$ at the given bulk strain rate of 10^{-5} s^{-1} cannot be explained by representing the fine-grained material within shear bands. Rather, an effect by a load-bearing framework of low strain lenses due to

insufficient connectivity and unfavourable orientation of shear bands is suggested to explain the observed bulk sample strengths. Bulk sample strength is interpreted to be determined by the combined rate of DPC and GBS in the coarse-grained low strain lenses and the fine-grained shear bands. The onset of DPC does not depend on the occurrence of shear bands but because diffusion lengths are proportional to the grain size, the rate of strain accommodation by DPC will vary strongly between fine grained shear bands compared to low strain lenses which largely preserve the coarse initial grain sizes. Delocalized viscous processes prior to shear band formation are also indicated by the lower initial slope of the loading curve in the mechanical data ([Figure 3a](#)), indicating a more viscous component of sample deformation from the start of the experiment. DPC is speculated to cause this viscous relaxation.

4.2.3 The influence of strain on reaction rate as seen from the microstructure

At 700 °C, fractures in Px porphyroclasts are extensively decorated by Amph overgrowths ([Figure 6](#)), where Amph is forming by the reaction:



Amph is seen to grow along Px-internal fractures with no contacting boundary towards Pl, indicating that element transport along the fractures occurred over several μm distance. It is described in the literature that fracturing can lead to high dislocation densities in the host crystal and is frequently associated with porosity (e.g. Fitz Gerald et al., 1991; Fitz Gerald and Stünitz, 1993; de Ronde et al., 2005). Fitz Gerald and Stünitz (1993) interpret from their observations that permeability along the microfractures must have been greatly enhanced, allowing for solution mass transport and mineral reactions along the fracture. Also from our observations, there is a clear positive feedback between deformation and reaction. This seems especially important in the 700 °C experiments, where the positive contribution of deformation on reaction rate is seen more strongly in the microstructure compared to 800 °C experiments. This is not unexpected, as reaction and diffusion rates will increase with increasing temperature and the

rate-enhancing effects of deformation on reaction and diffusion may become less important.

4.3 Linkage to natural faults

The findings from our experiments suggest that a transition from brittle to viscous deformation in the studied mafic rock type initiates where solution-mass transport processes occur at sufficiently high rates to accommodate deformation at the imposed strain rate. No significant contribution of crystal plastic processes could be observed. DPC and mineral reactions both take place simultaneously. The grain size reduction is caused primarily by mineral reaction and nucleation of new grains. The operation of DPC as a mechanism observed in our experiments depends on the metastability of minerals in the starting material. This situation is typical for most basalts and gabbros at amphibolite facies conditions and lower temperatures.

For the continental crust, with its lower geothermal heat gradient compared to the oceanic crust, mafic fault rocks at common strain rates ($< 10^{-9} \text{ s}^{-1}$) in the presence of fluids are likely to go through their brittle-viscous transition at much lower temperatures than observed in our experiments. Hydration reactions of feldspars at e.g. greenschist facies conditions can lead to grain size reduction and phase mixing, promoting viscous deformation by grain size sensitive creep mechanisms (e.g. Fitz Gerald and Stünitz, 1993; Stünitz and Fitz Gerald, 1993).

In the oceanic crust, where confining pressures (i.e. lithostatic pressures) are much lower for same temperatures compared to the continental crust, brittle-viscous transitional behaviour is likely to occur at higher temperatures, i.e. similar temperatures like in our experiments (e.g., Mehl and Hirth 2008). As pressures generally are lower, fracturing is will be more common and is likely contributing to deformation even to high temperatures.

As seen from our experiments, brittle-viscous transitional behaviour is not only a function of the externally applied parameters such as P and T, but especially a function of strain, i.e. microstructural evolution. This is an important factor to consider, as typically rheology of rocks is modelled as a material property without considering an evolution. We consider that this strain dependent rheology, as observed in our experiments, can be extrapolated to natural fault systems. Where

the strain dependency of rheology bears the potential to lead to a ‘time-dependent’ brittle-viscous transition as microstructure evolves towards favouring viscous deformation (as seen for the 700 °C experiments in our study).

5. Summary and conclusions

At the imposed experimental displacement rates, a transition from dominantly brittle to brittle-viscous to dominantly viscous is observed between the temperatures 600, 700 and 800 °C. The brittle-viscous transition in our study is observed to occur via a switch from fracturing to diffusion creep (in the sense of DPC) and grain boundary sliding as dominant viscous deformation mechanisms. Viscous deformation in our experiments starts with the onset of diffusive mass transport and starts to dominate the rheology when fine-grained, interconnected zones have formed.

The important processes enabling viscous rheology are 1) efficient solution-mass transport, 2) grain size refinement, which in our case as a result of reaction and nucleation, and 3) shear band interconnection.

We observe a brittle-viscous transition not only as a result of increasing temperatures but also via a microstructural evolution. Especially as the brittle-viscous transition is approached in terms of temperature (in our case at 700 °C), more evolved microstructure in shear bands allows for viscous deformation, whereas low strain lenses still show largely brittle deformation. This leads to a likely transient, mixed mechanical response of brittle and viscous rheology. For constant syn-kinematic conditions (i.e. strain rate, P and T, fluid availability, etc.) the syn-kinematic microstructural evolution with strain (and time) is expected to change the relative importance of brittle and viscous deformation in favour of the viscous processes.

Acknowledgements

We thank the team of the centre of nano imaging (SNI) at Basel University and Tom Eilertsen at Tromsø University for help and assistance with the electron microscopy. Terry Tullis is thanked for providing the Maryland Diabase material. Willy Tschudin is thanked for excellent thin section preparation. We gratefully acknowledge the funding provided by the Swiss National Foundation grant NF

200020_144448 and financial support from the Freiwillige Akademische
Gesellschaft, Basel, during the last stages of finishing this manuscript.

References

- Ashby, M.F., Verrall, R.A., 1973. Diffusion-accommodated Flow and Superplasticity. *Acta Metallurgica* 21.
- Boullier, A.M., Geugen, Y., 1975. SP-Mylonites: Origin of Some Mylonites by Superplastic Flow. *Contribution to Mineralogy and Petrology* 50, 93 – 104.
- Brace, W.F., Kohlstedt, D.L., 1980. Limits of Lithospheric Stress Imposed by Laboratory Experiments. *Journal of Geophysical Research* 85, 6248 – 6252.
- Bukovská, Z., Jerábek, P., Morales, L.F.G., 2016. Major softening at brittle-ductile transition due to interplay between chemical and deformation processes: An insight from evolution of shear bands in the South Armorican Shear Zone. *Journal of Geophysical Research* 121, 1158 – 1182.
- Burov, E.B., 2011. Rheology and strength of the lithosphere. *Marine and Petroleum Geology* 28, 1402–1443.
- Byerlee, J., 1978. Friction of Rocks. *Pure and Applied Geophysics* 116, 615–626.
- Byerlee, J.D., 1968. Brittle-ductile transition in rocks. *Journal of Geophysical Research* 73, 4741 – 4750.
- Byerlee, J.D., 1967. Frictional characteristics of granite under high confining pressure. *Journal of Geophysical Research* 72, 3639 – 3648.
- Bystricky, M., Mackwell, S., 2001. Creep of dry clinopyroxene aggregates. *Journal of Geophysical Research* 106(B7), 13443 – 13454.
- Carter, N.L., Tsenn, M.C., 1987. Flow properties of continental lithosphere. *Tectonophysics* 136, 27 – 63.
- Chen, S., Hiraga, T., Kohlstedt, D.L., 2006. Water weakening of clinopyroxene in the dislocation creep regime. *Journal of Geophysical Research* 111, B08203.
- Coble, R.L., 1963. A Model for Boundary Diffusion Controlled Creep in Polycrystalline Materials. *Journal of Applied Physics* 34, 1679 – 1682.
- de Ronde, A.A., Stunitz, H., Tullis, J., Heilbronner, R., 2005. Reaction-induced weakening of plagioclase-olivine composites. *Tectonophysics* 409, 85 – 106.

896 Dimanov, A., Dresen, G., 2005. Rheology of synthetic anorthite-diopside
897 aggregates: Implications for ductile shear zones. *Journal of Geophysical Research*
898 110, B07203.
899

900 Dimanov, A.E., Rybacki, E., Wirth, R., Dresen, G., 2007. Creep and strain-
901 dependent microstructures of synthetic anorthite-diopside aggregates. *Journal*
902 *of Structural Geology* 29, 1049 – 1069.
903

904 Dimanov, A., Lavie, M.P., Dresen, G., Ingrin, J., Jaoul, O., 2003. Creep of
905 polycrystalline anorthite and diopside. *Journal of Geophysical Research* 108,
906 B001815.
907

908 Drury, M.R., Avé Lallemant, H.G., Pennock, G.M., Palasse, L.N., 2011. Crystal
909 preferred orientation in peridotite ultramylonites deformed by grain size
910 sensitive creep, Étang de Lers, Pyrenees, France. *Journal of Structural Geology*
911 33, 1776 – 1789.
912

913 Drury, M.R., Humphreys, F., 1988. Microstructural shear criteria associated with
914 grain-boundary sliding during ductile deformation. *Journal of Structural Geology*
915 10, 83 – 89.
916

917 Elliott, D., 1973. Diffusion Flow Laws in Metamorphic Rocks. *Geological Society of*
918 *America Bulletin* 84, 2645–2664.
919

920 Fitz Gerald, J.D., Boland, J.N., McLaren, A.C., Ord, A., Hobbs, B., 1991.
921 Microstructures in water-weakened single crystals of quartz. *Journal of*
922 *Geophysical Research* 96, 2139 – 2155.
923

924 Fitz Gerald, J.D., Stünitz, H., 1993. Deformation of Granitoids at low Metamorphic
925 Grade. 1. Reactions and Grain-size Reduction. *Tectonophysics* 221, 269–297.
926

927 Fossen, H., Tikoff, B., 1993. The deformation matrix for simultaneous simple
928 shearing, pure shearing and volume change, and its application to transpression-
929 transtension tectonics. *Journal of Structural Geology* 15, 413 – 422.
930

931 Fousseis, F., Handy, M.R., 2008. Micromechanisms of shear zone propagation at
932 the brittle–viscous transition. *Journal of Structural Geology* 30, 1242–1253.
933

934 Gerbi, C., Johnson, S.E., Shulman, D., Klepeis, K., 2016. Influence of microscale
935 weak zones on bulk strength. *Geochemistry Geophysics Geosystems* 17, 4064 –
936 4077.
937

938 Getsinger, A.J., Hirth, G., 2014. Amphibole fabric formation during diffusion creep
939 and the rheology of shear zones. *Geology* 42, 535 – 538.
940

941 Gifkins, R.C., 1976. Grain-Boundary Sliding and its Accommodation During Creep
942 and Superplasticity. *Metallurgical Transactions* 7A, 1225 – 1232.
943

944 Goldsby, D., Tullis, T.E., 2002. Low frictional strength of quartz rocks at
 945 subseismic slip rates. *Geophysical Research Letters* 29, L015240.
 946
 947 Goncalves, P., Poilvet, J.-C., Oliot, E., Trap, P., 2016. How does shear zone
 948 nucleate? An example from the Suretta nappe (Swiss Eastern Alps). *Journal of*
 949 *Structural Geology* 86, 166 – 180.
 950
 951 Gratier, J.-P., Dysthe, D.K., Francois, R., 2013. The Role of Pressure Solution Creep
 952 in the Ductility of the Earth's Upper Crust, in: Dmowska, R. (Ed.), *Advances in*
 953 *Geophysics*. pp. 47 – 179.
 954
 955 Gratier, J.-P., Guiguet, R., Renard, F., Jenatton, L., Bernard, D., 2009. A pressure
 956 solution creep law for quartz from indentation experiments. *Journal of*
 957 *Geophysical Research* 114, B03403.
 958
 959 Gratier, J.-P., Richard, J., Renard, F., Mittempergher, S., Doan, M.-L., Di Toro, G.,
 960 Hadizadeh, J., Boullier, A.-M., 2011. Aseismic sliding of active faults by pressure
 961 solution creep: Evidence from the San Andreas Fault Observatory at Depth.
 962 *Geology* 39, 1131–1134.
 963
 964 Green, H. W. II, Borch, R. S., 1989. A new molten salt cell for precision stress
 965 measurements at high pressure. *Eur. J. Miner.* 1, 213 - 219.
 966
 967 Griggs, D.T., Turner, F.J., Heard, H.C., 1960. Deformation of rocks at 500 to 800°C.
 968 *Geol. Soc. Am., Mem.* 79, 39 – 105.
 969
 970 Hacker, B.R., Christire, J.M., 1991. Experimental deformation of a glassy basalt.
 971 *Tectonophysics* 200, 79 – 96.
 972
 973 Handin, J., 1966. Strength and ductility, in: Clark, S.P. (Ed.), *Handbook of Physical*
 974 *Constants*, *Geol. Soc. Am. Mem.* pp. 223 – 289.
 975
 976 Hawthorne, F. C., Oberti, R., Harlow, G. E., Maresch, W. V., Martin, R. F.,
 977 Schumacher, J. C., and Welch, M. D., 2012. Nomenclature of the amphibole
 978 supergroup. *American Mineralogist* 97, 2031 – 2048
 979
 979 Heard, H.C., 1960. , in: Griggs, D.T., Handin, J. (Eds.), *Transition from Brittle*
 980 *Fracture to Ductile Flow in Solnhofen Limestone as a Function of Temperature,*
 981 *Confining Pressure and Interstitial Fluid Pressure, Rock Deformation, Mem. Geol.*
 982 *Soc. Am. New York*, pp. 193 – 226.
 983
 984 Heilbronner, R., Barrett, S., 2014. *Image Analysis in Earth Sciences -*
 985 *Microstructures and Textures of Earth Materials.* Springer-Verlag, Berlin.
 986
 987 Holyoke III, C.W., Kronenberg, A.K., 2010. Accurate differential stress
 988 measurement using the molten salt cell and solid salt assemblies in the Griggs
 989 apparatus with applications to strength, piezometers and rheology.
 990 *Tectonophysics* 494, 17 – 31.
 991

992 Janssen, C., Wirth, R., Rybacki, E., Naumann, R., Kemnitz, H., Wenk, H.-R., Dresen,
 993 G., 2010. Amorphous material in SAFOD core samples (San Andreas Fault):
 994 Evidence for crush-origin pseudotachylytes? *Geophysical Research Letters* 37,
 995 L01303.
 996
 997 Karato, S.-I., 2008. *Deformation of Earth Materials - an introduction to the*
 998 *rheology of solid earth*. Cambridge University Press, Cambridge.
 999
 1000 Keulen, N., Heilbronner, R., Stünitz, H., Boullier, A.-M., Ito, H., 2007. Grain size
 1001 distributions of fault rocks: A comparison between experimentally and naturally
 1002 deformed granitoids. *Journal of Structural Geology* 29, 1282 – 1300.
 1003
 1004 Kilian, R., Heilbronner, R., Stünitz, H., 2011. Quartz grain size reduction in a
 1005 granitoid rock and the transition from dislocation to diffusion creep. *Journal of*
 1006 *Structural Geology* 33, 1265–1284.
 1007
 1008 Kohlstedt, D.L., Evans, B., Mackwell, S.J., 1995. Strength of the Lithosphere:
 1009 Constraints imposed by laboratory experiments. *Journal of Geophysical Research*
 1010 100 (17), 517–587

 1011 Kohlstedt, D.L., Hansen, L.N., 2015. Constitutive equations, rheological behavior,
 1012 and viscosity of rocks, in: Schubert, G. (Ed.), *Treatise on Geophysics*. Elsevier,
 1013 Oxford, pp. 441 – 472.
 1014
 1015 Kronenberg, A.K., Shelton, G.L., 1980. Deformation microstructures in
 1016 experimentally deformed Maryland Diabase. *Journal of Structural Geology* 2, 341
 1017 – 353.
 1018
 1019 Mackwell, S.J., 1991. High-temperature creep of enstatite single crystals.
 1020 *Geophysical Research Letters* 18, 2027 – 2030.
 1021
 1022 Mancktelow, N.S., Pennacchioni, G., 2005. The control of precursor brittle
 1023 fracture and fluid–rock interaction on the development of single and paired
 1024 ductile shear zones. *Journal of Structural Geology* 27, 645 – 661.
 1025
 1026 Panozzo Heilbronner, R., 1984. Two-dimensional strain from the orientation of
 1027 lines in a plane. *Journal of Structural Geology* 6, 215 – 221.
 1028
 1029 Paterson, M.S., 2013. *Materials Science for Structural Geology*. Springer,
 1030 Dordrecht.
 1031
 1032 Paterson, M.S., Wong, T.-F., 2005. *Experimental Rock Deformation – The Brittle*
 1033 *Field*, 2nd ed. Springer, Berlin Heidelberg.
 1034
 1035 Pec, M., Stünitz, H., Heilbronner, R., Drury, M., 2016. Semi-brittle flow of granitoid
 1036 fault rocks in experiments. *Journal of Geophysical Research Solid Earth* 121,
 1037 B012513.
 1038

1039 Pec, M., Stünitz, H., Heilbronner, R., Drury, M., de Capitani, C., 2012. Origin of
1040 pseudotachylites in slow creep experiments. *Earth and Planetary Science Letters*
1041 355-356, 299 – 310.
1042
1043 Pennacchioni, G., Mancktelow, N., 2007. Nucleation and initial growth of a shear
1044 zone network within compositionally and structurally heterogeneous granitoids
1045 under amphibolite facies conditions. *Journal of Structural Geology* 29, 1757–
1046 1780.
1047
1048 Price, N.A., Johnson, S.E., Gerbi, C.C., West Jr., D.P., 2012. Identifying deformed
1049 pseudotachylite and its influence on the strength and evolution of a crustal
1050 shear zone at the base of the seismogenic zone. *Tectonophysics* 518-521, 63 s
1051 518
1052
1053 Raterron, P., Jaoul, O., 1991. High-temperature deformation of diopside single
1054 crystal, 1. mechanical data. *Journal of Geophysical Research* 96, 14277 – 14286.
1055
1056 Richter, B., Stünitz, H., Heilbronner, R., 2016. Stresses and pressures at the
1057 quartz-to-coesite phase transformation in shear- deformation experiments.
1058 *Journal of Geophysical Research Solid Earth* 121, B013084.
1059
1060 Rutter, E.H., 1976. The kinetics of rock deformation by pressure solution.
1061 *Philosophical Transactions of the Royal Society of London* 283, 203 – 219.
1062
1063 Rutter, E.H., Peach, C.J., White, S.H., Johnston, D., 1985. Experimental
1064 “syntectonic” hydration of basalt. *Journal of Structural Geology* 7, 251 – 266.
1065
1066 Rybacki, E., Dresen, G., 2000. Dislocation and diffusion creep of synthetic
1067 anorthite aggregates. *Journal of Geophysical Research* 105, 26017 – 26036.
1068
1069 Rybacki, E., Gottschalk, M., Wirth, R., Dresen, G., 2006. Influence of water fugacity
1070 and activation volume on the flow properties of fine-grained anorthite
1071 aggregates. *Journal of Geophysical Research* 111, B03203.
1072
1073 Schmid, S., Panozzo, R., Bauer, S., 1987. Simple shear experiments on calcite
1074 rocks: rheology and microfabric. *Journal of Structural Geology* 9, 747 – 778.
1075
1076 Shelton, G., Tullis, J., Tullis, T., 1981. Experimental high temperature and high
1077 pressure faults. *Geophysical Research Letters* 8, 55 – 58.
1078
1079 Sibson, R.H., 1984. Roughness at the Base of the Seismogenic Zone: Contributing
1080 Factors. *Journal of Geophysical Research* 89, 5791 – 5799.
1081
1082 Sibson, R.H., 1982. Fault zone models, heat flow, and the depth distribution of
1083 earthquakes in the continental crust of the United States. *Bulletin of the*
1084 *Seismological Society of America* 72, 151 – 163.
1085
1086 Simpson, C., 1986. Fabric Development in Brittle-to-Ductile Shear Zones. *Pure*
1087 *and Applied Geophysics* 124, 269–288.

1088
1089 Stel, H., 1981. Crystal growth in cataclasites: Diagnostic microstructures and
1090 implications. *Tectonophysics* 78, 585 – 600.
1091
1092 Storti, F., Billi, A., Salvini, F., 2003. Particle size distributions in natural carbonate
1093 fault rocks: insights for non-self-similar cataclasis. *Earth and Planetary Science*
1094 *Letters* 206, 173 – 186.
1095
1096 Stünitz, H., Fitz Gerald, J.D., 1993. Deformation of granitoids at low metamorphic
1097 grade. II: Granular flow in albite-rich mylonites. *Tectonophysics* 221, 229 – 324.
1098
1099 Trepmann, C.A., Stöckert, B., 2003. Quartz microstructures developed during
1100 non-steady state plastic flow at rapidly decaying stress and strain rate. *Journal of*
1101 *Structural Geology* 25, 2035 – 2051.
1102
1103 Tullis, J., Yund, A., 1987. Transition from cataclastic flow to dislocation creep of
1104 feldspar: Mechanisms and microstructures. *Geology* 15, 606 – 609.
1105
1106 Tullis, J., Yund, R.A., 1977. Experimental deformation of dry Westerly granite.
1107 *Journal of Geophysical Research* 82, 5705 – 5718.
1108
1109 Yund, R.A., Blanpied, M.L., Tullis, T.E., Weeks, J.D., 1990. Amorphous material in
1110 high strain experimental fault gauges. *Journal of Geophysical Research* 95, 15589
1111 – 15602.
1112
1113
1114
1115
1116
1117
1118
1119

Figure Captions

Figure 1 : Sample assembly. a) Schematic cross-section of sample assembly. Inset shows details on sample. b) Thin section of sample 449 after deformation. Black arrow indicates unloading crack. FB = forcing block, SZ = shear zone.

Figure 2 : Reference frame and definitions. a) Micrographs are oriented with the shear zone boundaries parallel to the x-direction with a dextral sense of shear. b) In rose diagrams, preferred orientations are marked with black dots; θ = angle between orientation and applied load (σ_1 direction); Φ = angle between orientation and shear plane (shear zone boundaries). c) Stresses are plotted as shear stress τ versus apparent shear strain γ_a , see Appendix. Stages of the experiment are indicated.

Figure 3 : Mechanical data. a) Shear stress vs. apparent shear strain for experiments performed at $T = 600, 700$ and 800 °C, using confining pressures (P_c) of $\sim 0.5, 1.0$ and 1.5 GPa. Shear strain rate for all experiments is $\sim 3 \times 10^{-5} \text{ s}^{-1}$. b) Mohr diagrams for same experiments. σ_3 = confining pressure; σ_1 = yield stress. (black lines) or quasi-steady state (grey dotted lines). In red, apparent friction coefficient μ' and angle of internal friction. μ' values decrease with increasing T and increasing P_c . Stress values usually stay below Byerlees relationship except for 600 and 700 °C experiments at $P_c = 0.5$ GPa.

Figure 4 : Derivation of stress exponents. a) Shear stress vs. apparent shear strain rate, with calculated stress exponent n ; slope of linear fit is $1/n$. b) Different stress exponents calculated for different data-correction routines shown for two experiments performed at $T = 800$ °C / $P_c = 1.0$ GPa and $T = 300$ °C / $P_c = 0.5$ GPa. R16 = after Richter et al., 2016; H&K10 = after Holyoke & Kronenberg, 2010; P12 = after Pec et al, 2012 (see Methods).

Figure 5 : Microstructure development across the brittle-viscous transition. Experimental conditions are indicated, dextral shear sense applies to all. a) and b) At $T = 600$ °C, fracturing is extensive; a foliation (S) is developed by cataclastic

flow; shear displacement is accommodated along shear bands and shear fractures in Riedel shear (R) orientations. c) Pore trails along fractures indicate partial healing. d) and e) At $T=700\text{ }^{\circ}\text{C}$, fracturing is extensive in Px porphyroclasts; a foliation (S) is developed partly by cataclastic flow. e) Shear bands are recognized by a fine-scale compositional layering and intense grain size reduction; hydrous reaction products Amph and Zo are beginning to form. f) and g) At $T = 800\text{ }^{\circ}\text{C}$, broad shear bands (white stippled lines) anastomose around low strain lenses; they are characterized by grain size reduction and the formation of a foliation parallel to the shear band boundaries; hydrous reactions products Amph and (to a lower extent) Zo are formed.

Figure 6 : Hydrous reactions at $700\text{ }^{\circ}\text{C}$. Left: digitally produced phase maps, right, BSE image of the same area. Dark grey = Pl; orange = Amph; bright grey = Px ; sample deformed at $T = 700\text{ }^{\circ}\text{C}$, $P_c = 1.0\text{ GPa}$. Amph follows zones of high strain such as shear bands, or fractures within Px clasts.

Figure 7 : Shear band morphology as a function of temperature. Shear bands and shear fractures are traced in red. Light background layer are BSE contrast images of the shear zones. Rose diagrams (surface ODFs) show orientation of boundary segments of the traced structures. Horizontal shear bands developed at the forcing block-shear zone interface are omitted from the analysis. Rose diagrams show the dominance of more shear zone parallel shear bands at higher experimental T . b) Shear band width distributions. Shear bands stay largely below $10\text{ }\mu\text{m}$ at $600\text{ }^{\circ}\text{C}$, and get broader at higher T , reaching up to $70\text{ }\mu\text{m}$ for the presented $800\text{ }^{\circ}\text{C}$ experiment.

Figure 8 : Micro- to nanostructures of shear bands developed at $600\text{ }^{\circ}\text{C}$. a) SEM BSE image of a shear band formed in the sample near interface with the forcing block; shear sense is dextral. b) - d) TEM images of a shear band similar to the one shown in a). Kinematic reference frame for images b) - d) is given in upper right corner in b). b) BF TEM image. Increasing grain size refinement from top to lower half of the image; cryst = crystalline; amor = amorphous. Note few remaining crystals (darker) within amorphous layers. c) HAADF (left) and BF

TEM image (right) of nano-crystals mainly formed by Px; amorphous layers correlate with the typical darker grey-value of Pl. d) High-resolution BF image from a central part of the shear band; nano-crystalline layer enclosed between amorphous domains. White squares denote areas where diffraction spots are detected in FFT analyses (see Methods); locally, amorphous layers contain nano-crystals, identified both from diffraction spots in FFT images and from their dark appearance in the BF image.

Figure 9 : Micro- to nanostructures of shear bands developed at 700 °C. a) SEM BSE image of a shear band. b) SE SEM image of the surface of a shear band; mostly Pl grains are visible; white arrow indicates shear direction, with top to the upper right. c) HAADF image showing a Px porphyroclast adjacent to a fine grained shear band formed by Pl + Amph; the Px porphyroclast shows a thin reaction corona of Amph; black arrow points to porosity within the Px clast. d) HAADF image of a Pl porphyroclast with surrounding fine-grained Pl in a shear band; the trace of an EDS profile is marked. Kinematic reference frame is the same as in c). e) Element counts of Si, Ca and Al (normalized to max. count value of the respective element) versus distance (pixel) along the profile marked in d); mean values (blue) are indicated for the porphyroclast and the Pl of the shear band.

Figure 10 : Micro- to nanostructures of shear bands developed at 800 °C. a) SE BSE image of a shear band with typical compositional layering of Pl dominated layers alternating with Amph+Qz(+Pl) mixed layers. b) BF TEM image of Pl grains within a shear band; grains show a low defect density; porosity is low and grain boundaries are tight. c) HAADF image showing the typical compositional layering of Pl dominated layers alternating with Amph+Qz aggregates. d) BF-STEM image of the same area as in c).

Figure 11 : Shape of plagioclase grains in shear bands at 800 ° C. a) BF TEM image of diamond-shaped Pl grains with a weak shape preferred orientation. b) Rose diagram (surface ODF) of Pl grain boundaries preferentially oriented at $\Phi = 10\text{-}30^\circ$. The ODF shows a weak anisotropy consistent with the dextral sense

of shear. c) Grain boundary segments are visualized separately for horizontal ($30^\circ < \Phi < 30^\circ$) and vertical ($30^\circ < \Phi < 150^\circ$) orientations (marked black in rose diagrams).

Figure 12 : Grain size distribution of plagioclase in shear bands. a) Sample 416 deformed at $T = 700^\circ\text{C}$, $P_c = 1.0\text{ GPa}$; area equivalent grain diameters, d_{equ} , were determined from SE images as shown in Fig. 9b. b) Sample 414 deformed at $T = 800^\circ\text{C}$, $P_c = 1.0\text{ GPa}$; area equivalent grain diameters, d_{equ} , were determined from TEM images of the FIB-foil shown in Fig. 10. Dark grey bars represent $>80\%$ of all grains; black line = kernel density estimate fit, number of grains, n , and mode of curve fit are indicated.

Figure 13 : Evolution of shear bands with increasing strain. a) Central parts of shear zones deformed at $T = 800^\circ\text{C}$ and $P_c = 1.0\text{ GPa}$ to increasing apparent shear strains; sample 449 ($P_c = 1.5\text{ GPa}$) is included for comparison. Shear bands are shown in orange; rose diagrams with surface ODF of shear band boundary segments on right. With increasing strain, dominant shear band orientation becomes more shear zone parallel and shear bands become wider and better interconnected. b) Stress - strain curves for samples shown in a). c) Increase of area fraction of shear bands with increasing shear strain. Although geometry of shear bands at 1.0 and 1.5 GPa differ, their area-% is identical..

Figure 14 : Zones of initial shear localization. BSE SEM image of sample 460 deformed at $T = 800^\circ\text{C}$, $P_c = 1.0\text{ GPa}$. Black arrows point to minute segregation of melt; nucleation of new Amph (white arrow) and Pl grains is observed.

Figure 15 : Comparison of shear band orientation formed at peak stress (left) and at higher strains at quasi steady state. Rose diagrams are surface ODFs of shear zone boundary segments. Initiation of shear band shows comparable preferred angles for all temperatures. At higher temperatures however, shear band orientations are more shear zone parallel with increasing strain, i.e. microstructural evolution.

1252 **Table 1** : Composition of Maryland Diabase starting material. EDS
1253 measurements as oxide wt.-% and calculated to stoichiometric mineral formula.
1254

1255 **Table 2** : List of experiments and experimental conditions.

1256 T = Temperature
1257 Pc = Confining pressure, averaged between $\gamma_a = 1.5$ to end of experiment;
1258 (*) denotes peak stress experiments where average Pc is calculated between
1259 beginning and end of experiment.
1260 Peak τ = Maximum shear stress.
1261 Flow τ = Shear stress during quasi-steady state or at end of experiment.
1262 γ_a = Total apparent shear strain.
1263 $\dot{\gamma}_a$ = Apparent shear strain rate: (1) constant displacement rate
1264 experiments. $\dot{\gamma}_a$ calculated as the average value between $\gamma_a = 1.5$ and end
1265 of experiment; (2) displacement rate stepping tests. $\dot{\gamma}_a$ as average value
1266 for each setting.

1267

1268 **Appendix Figure 1** : General shear setup within initial state and shear zone
1269 thickness, th0, and state at end of experiment and final shear zone thickness, thF.
1270 For representation purposes, the displacement is displayed to occur asymmetric
1271 by shift of only the upper forcing block.

1272 **Appendix Table 1** : Different measures for shear strain.

1273 th0 = estimated shear zone thickness at start of experiment (Appendix Figure 2).
1274 thF = measured shear zone thickness at end of experiment (Appendix Figure 1).
1275 d = axial displacement of σ_1 -piston.
1276 sdF = displacement of σ_1 -piston parallel to shear zone boundary (Appendix
1277 Figure 1).
1278 $k = th0/thF$ = pure shear component.
1279 $thF/th0$ (%) = relative thickness of sample after deformation.
1280 Γ_{eff} = effective shear strain (Appendix Eq. (A4)).
1281 γ_{TH} = shear strain determined from relative displacement of forcing blocks as
1282 measured on thin sections.

1283 γ_{comp} = simple shear component (Appendix Eq. (A5)).
 1284 γ_{a} = apparent shear strain (Appendix Eq. (A2)).
 1285 R_f = aspect ratio of finite strain ellipse (after Fossen & Tikoff, 1973).
 1286 ϕ = orientation of finite stretching direction (after Fossen and Tikoff, 1973).
 1287 ε_{m} = strain magnitude (Appendix Eq. (A6)).

1288

1289

1290 **Appendix**

1291 *A1. Derivation of shear strains*

1292 General shear experiments like the ones described in this paper often experience
 1293 sample thinning, even if the samples are pre-compacted or annealed before the
 1294 actual start of the shear deformation. Thinning continues throughout the
 1295 experiments, as inferred from samples deformed under identical conditions to
 1296 different total strains. It is usually observed that the sample material does not
 1297 escape sideways. The strain is therefore taken to be plane strain and calculations
 1298 are made in 2 dimensions by assuming a combination of pure shear (thinning of
 1299 shear zone) and simple shear (displacement parallel to the piston-sample
 1300 interface).

1301 Measurements indicate that the samples thin linearly from the beginning of the
 1302 experiment to the end. Correlating the shear zone thickness, thF , with the axial
 1303 displacement, d , a linear trend of shear zone thinning is evident ([Appendix Figure](#)
 1304 [1](#)). The initial thickness, i.e., the thickness of the compacted samples at the start of
 1305 the experiment, depends on temperature. Two initial thicknesses for $T = 800^\circ\text{C}$ and
 1306 $T \leq 700^\circ\text{C}$ are derived ([Appendix Table 1](#)).

1307 For strain calculations, the axial displacement, d , of the σ_1 -piston is partitioned
 1308 into a shear component parallel to the 45° sample piston interface, and a thinning
 1309 component normal to the shear zone boundary. Dividing the total shear
 1310 displacement sdF , by the final thickness thF , γ_{TH} is derived ([Appendix Figure 2](#)).

1311

$$1312 \quad \gamma_{\text{TH}} = sdF / thF \quad (A1a)$$

$$1313 \quad sdF = (d - (th0 - thF) \cdot \cos(45^\circ)) / \cos(45^\circ) \quad (A1b)$$

1314

where: sdF : total displacement parallel to the piston-sample interface; $th0 / thF$: initial / final thickness of sample.

In this study, the shear strain is calculated from the experimental record as the sum of individual increments of shear displacement divided by the instantaneous shear zone thickness. The shear strain derived in this manner is referred to as apparent shear strain γ_a :

$$\gamma_a(k) = \sum_{i=2}^k \frac{sd(i) - sd(i-1)}{th(i)} \quad (A2)$$

$sd(i)$: displacement along piston-sample interface; $th(i)$: shear zone thickness at time i . The shear strain values calculated in this fashion depend on the thinning of the sample. γ_a is termed 'apparent', as it is not a real measure of simple shear.

The pure shear component of the sample strain is calculated as

$$k = th0 / thF \quad (A3)$$

Following Fossen and Tikoff (1993), the effective shear strain, Γ_{eff} , and the simple shear strain component, γ_{comp} , are derived as

$$\Gamma_{eff} = k^{-1} \cdot \tan(\psi) = sdF / th0 \quad (A4)$$

$$\gamma_{comp} = \Gamma_{eff} \cdot \frac{2 \ln(k)}{k - k^{-1}} \quad (A5)$$

The difference between the strain measures is small as shown in [Appendix Figure 3](#). Note that, if $thF = th0$, i.e., if $k = 1$, all strain measures coincide: $\gamma_{TH} = \gamma_a = \Gamma = \gamma_{comp}$. In order to be able to convert from axial to shearing experiments, the strain magnitude is derived after Schmid et al. (1987):

$$\varepsilon_m = \frac{1}{\sqrt{3}} [(\varepsilon_1 - \varepsilon_2)^2 + (\varepsilon_2 - \varepsilon_3)^2 + (\varepsilon_3 - \varepsilon_1)^2]^{1/2} \quad (A6)$$

1345 where ε_m = strain magnitude; $\varepsilon_1, \varepsilon_2, \varepsilon_3$ = axes of the strain ellipsoid calculated
1346 after Fossen and Tikoff (1993). Plane strain conditions are assumed with $\varepsilon_2 = 1$.
1347
1348